Spin dynamical properties and orbital states of the layered perovskite La2-2xSr1+2xMn207 (0.3?x<0.5)

doi: 10.1103/PhysRevB.65.064414

Spin dynamical properties and orbital states of the layered perovskite $La_{2-2x}Sr_{1+2x}Mn_2O_7$ $(0.3 \leqslant x < 0.5)$

K. Hirota,[1,*] S. Ishihara,[2,†] H. Fujioka,[1,‡] M. Kubota,[3,§] H. Yoshizawa,[3] Y. Moritomo,[4] Y. Endoh,[5] and S. Maekawa[5]
[1]*Department of Physics, Tohoku University, Sendai 980-8578, Japan*
[2]*Institute for Materials Research, Tohoku University, Sendai 980-8577, Japan*
[3]*Neutron Scattering Laboratory, Institute for Solid State Physics, University of Tokyo, Tokai 319-1106, Japan*
[4]*Center for Integrated Research in Science and Engineering, Nagoya University, Nagoya 464-8601, Japan*
[5]*CREST, Institute for Materials Research, Tohoku University, Sendai 980-8577, Japan*
(Received 27 April 2001; revised manuscript received 20 September 2001; published 16 January 2002)

Low-temperature spin dynamics of the double-layered perovskite $La_{2-2x}Sr_{1+2x}Mn_2O_7$ (LSMO327) was systematically studied in a wide hole concentration range $(0.3 \leqslant x < 0.5)$. The spin-wave dispersion, which is almost perfectly two-dimensional, has two branches due to a coupling between layers within a double-layer. Each branch exhibits a characteristic intensity oscillation along the out-of-plane direction. We found that the in-plane spin stiffness constant and the gap between the two branches strongly depend on x. By fitting to calculated dispersion relations and cross sections assuming a Heisenberg model, we have obtained the in-plane ($J_{\parallel}$), *intra*-bilayer ($J_{\perp}$) and *inter*-bilayer (J') exchange interactions at each x. At $x=0.30$, $J_{\parallel}=-4$ meV and $J_{\perp}=-5$ meV, namely almost isotropic and ferromagnetic. Upon increasing x, $J_{\perp}$ rapidly approaches zero while $|J_{\parallel}|$ increases slightly, indicating an enhancement of the planar magnetic anisotropy. At $x=0.48$, $J_{\parallel}$ reaches -9 meV, while $J_{\perp}$ turns to $+1$ meV, indicating an antiferromagnetic interaction. Such a drastic change of the exchange interactions can be ascribed to the change of the relative stability of the $d_{x^2-y^2}$ and $d_{3z^2-r^2}$ orbital states upon doping. However, a simple linear combination of the two states results in an orbital state with an orthorhombic symmetry, which is inconsistent with the $I4/mmm$ tetragonal symmetry of the crystal structure. We thus propose that an ''orbital liquid'' state realizes in LSMO327, where the charge distribution symmetry is kept tetragonal around each Mn site. Orbital liquid states are formulated in a theoretical model which takes into account strong electron correlations. The calculated results satisfactorily explain the systematic changes of the exchange interactions in LSMO327 observed in the experiments.

DOI: 10.1103/PhysRevB.65.064414 PACS number(s): 75.30.Ds, 75.30.Et, 61.12.−q, 75.10.−b

I. INTRODUCTION

Rare-earth doped Mn perovskite oxide $R_{1-x}A_xMnO_3$ (R: rare-earth ion; A: alkaline-earth ion) is a prototype of the colossal magnetoresistance (CMR) materials. Considerable amounts of efforts have been made to clarify the magnetic, electrical, and structural properties of these systems.[1–10] It has become recognized that the complex and delicate balance among the internal degrees of freedom of electrons, i.e., charge, spin, and orbital, is a key to understand the physics of these materials.[10,11] In the Mn perovskite oxides, the orbital degree of freedom arises from an electron in the doubly degenerated e_g states of a Mn^{3+} ion in a MnO_6 octahedron. Comparing with the charge and spin degrees of freedom, however, the orbital degree of freedom has been much less explored, partially due to lack of experimental techniques to *directly* measure the ordering processes and the states, with the exception of a pioneering work by Akimitsu and Ito who have established the orbital ordered state in K_2CuF_4 by measuring the anisotropy of the magnetic form factor using polarized neutrons.[12] Recently, resonant x-ray scattering techniques were successfully applied to the detection of the orbital ordering process in $La_{0.5}Sr_{1.5}MnO_4$,[13] which was a significant step toward the understanding of the ''third'' degree of freedom of electrons. In the case of $LaMnO_3$, the resonant x-ray scattering techniques have provided direct evidence of the orbital ordering.[14] Two-dimensional (2D) planar ferromagnetic coupling found in this three-dimensional (3D) lattice can be naturally explained by this orbital ordering.[15–18]

$R_{1-x}A_xMnO_3$ consists of corner sharing MnO_6 octahedra which are three-dimensionally connected. Due to mismatch of ionic radii of Mn and $(R_{1-x}A_x)$ ions, the Mn–O–Mn bond angle deviates from 180°, which is called buckling.[19] Since doping holes inevitably alter the average ionic radius of an $(R_{1-x}A_x)$ ion, the amount of buckling also changes, resulting in a variety of crystal structures.[20] Structural phase transitions are also observed with changing temperature,[5,21] and can be induced by an external magnetic field.[22] The complexity of structural properties of $R_{1-x}A_xMnO_3$ is an interesting issue,[23] but makes it difficult to study the role and significance of the orbital degree of freedom in the magnetic and transport properties, because orbitals are strongly affected by surrounding structural environment.

Mn perovskite oxides are generally represented by the Ruddlesden–Popper notation $(R,A)_{n+1}Mn_nO_{3n+1}$, where the effective dimensionality can be adjusted by changing the number of MnO_2 sheets, n, blocked with $(R,A)_2O_2$ layers. As for the double-layered Mn perovskite $(n=2)$, Moritomo *et al.*[24] have found an extremely large magnetoresistance around the Curie temperature T_C in a single crystal of $La_{1.2}Sr_{1.8}Mn_2O_7$, which was followed by intensive studies of $La_{2-2x}Sr_{1+2x}Mn_2O_7$ (LSMO327) and related compounds.[25] Figure 1 schematically shows the structure and the magnetically ordered state at $x=0.40$.[26] A comprehensive magnetic

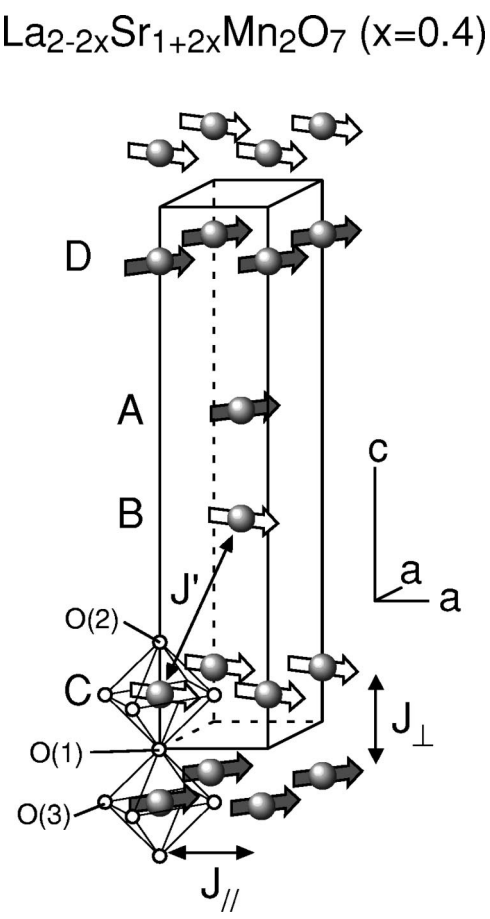

FIG. 1. Schematic representation of the magnetic spin arrangement on Mn ions in the $I4/mmm$ tetragonal cell of $La_{1.2}Sr_{1.8}Mn_2O_7$. Each Mn ion is surrounded by an O_6 octahedron. The lattice parameters are $a=b=3.87$ and $c=20.1$ Å at 10 K (Ref. 26). Notations are explained in Sec. IV.

and structural phase diagram of LSMO327 has been established by Kubota *et al.*[27,28] in a wide range of x ($0.30 \leqslant x \leqslant 0.50$) through systematic powder neutron-diffraction studies combined with the Rietveld analysis. They have found that LSMO327 exhibits a planar ferromagnetic (FM) structure FM-I in the range $0.32 \leqslant x \leqslant 0.38$ at low temperatures and that a finite canting angle between neighboring layers starts appearing around $x \sim 0.39$ and reaches 180° (AFM-I, i.e., A-type AFM) for $x \geqslant 0.48$. They also found that the magnetic moments are aligned parallel to the c-axis at $x=0.30$, indicating a phase boundary between $x=0.30$ and 0.32. At $x=0.50$, the magnetic structure exhibits complicated temperature dependence due to charge ordering.[29,30]

In contrast to the rich magnetic phase diagram, the structure of LSMO327 is fairly simple. Although anomalous structural behaviors were reported around T_C suggesting a strong coupling among charge, spin and lattice,[31,32] there is only a single tetragonal ($I4/mmm$) phase in the entire hole concentration ($0.30 \leqslant x \leqslant 1.0$) and temperature ranges ($T \leqslant 400$ K) studied so far, except a recently discovered orthorhombic ($Immm$) phase which exists in a limited concentration range ($0.75 < x < 0.95$).[33] This simplicity is most likely due to the layered structure itself which absorbs the changes of the Mn–O bond lengths and the average ionic radii of La and Sr ions upon doping. It was also found that the Jahn–Teller (JT) type lattice distortion Δ_{JT} of Mn-O_6 octahedra monotonically changes with increasing x.[28] Note that Δ_{JT} here is defined by the ratio of the averaged apical Mn–O bond length to the equatorial Mn–O bond length, i.e., $\Delta_{JT} \equiv (d_{Mn-O(1)}+d_{Mn-O(2)})/2d_{Mn-O(3)}$, where d_{Mn-O} is a distance between nearest neighbor (NN) Mn and O ions. The positions of the O ions are depicted in Fig. 1. The results are in good agreement with x-ray diffraction measurements.[36,37] The JT distortion in LSMO327 stabilizes either $d_{x^2-y^2}$ or $d_{3z^2-r^2}$ state. The contraction of MnO_6 octahedra upon doping implies the stabilization of the $d_{x^2-y^2}$ state, i.e., a pseudo-2D e_g band, in a heavily doped region. As discussed later, such a structural change itself cannot account for the systematic changes of the exchange interactions within the conventional double exchange scenario. The dominance of the A-type AFM structure with the decrease of Δ_{JT} is ascribed to the change in the e_g orbital state from $d_{3z^2-r^2}$ to $d_{x^2-y^2}$.[26,28] The importance of the e_g orbital state was also pointed out in striction measurements by Kimura *et al.*[34] as well as Argyriou *et al.*[32] and Medarde *et al.*[35]

The dynamical magnetic properties of LSMO327 with $x=0.4$ were measured by Fujioka *et al.*[38] They found that the spin wave dispersion is almost perfectly 2D with the in-plane spin stiffness constant $D \sim 151$ meV Å . This value is similar to that of $La_{1-x}Sr_xMnO_3$ (LSMO113) with $x \sim 0.3$, though T_C of LSMO113 is three times higher. They found that there exist two branches due to a coupling between layers *within* a double-layer. They have analyzed the spin-wave dispersion and the differential scattering cross section by applying the Holstein–Primakoff transformation to a Heisenberg Hamiltonian with in-plane $J_{\|}$ and *intra*-bilayer $J_{\perp}$ interactions (see Fig. 1). They have estimated that the *intra*-bilayer coupling is ~30% of the in-plane coupling, which is contrary to the fact that the Mn–O bond lengths are similar. They speculated that the $d_{x^2-y^2}$ orbital is dominant at $x=0.40$, which enhances the double-exchange, i.e., ferromagnetic, interaction within the planes. This interpretation is consistent with the conclusion drawn by previous structural studies.[27,28] The l-dependence of the scattering intensity due to the spin wave shows an excellent agreement with the theoretical calculation of the differential scattering cross section. Similar inelastic neutron-scattering experiments were independently performed by Chatterji *et al.*,[39] which gives consistent results with that of Fujioka *et al.*[38] The low-energy spin-wave excitations were measured by Chatterji *et al.*[40] and Rosenkranz *et al.*,[41] which revealed the *inter*-bilayer exchange interaction as well as the anisotropy gap at $x=0.40$.

The importance of the e_g orbital state in determining the magnetic and transport properties of LSMO327 is clear. Moreover, its simple structure makes LSMO327 more favorable platform to study the roles of orbital degree of freedom than LSMO113. The resonant x-ray scattering technique, however, is not directly applicable to LSMO327 because the superlattice reflections resulting from an antiferro-type orbital ordering, as seen in $LaMnO_3$, is not expected to be seen in LSMO327 in the $0.30 \leqslant x < 0.5$ range. Instead, it is necessary to determine the e_g orbital polarization. In the present

study, we have carried out a series of inelastic neutron-scattering measurements on single crystals of the layered perovskite $La_{2-2x}Sr_{1+2x}Mn_2O_7$ at $x=0.30$, 0.35, 0.40, and 0.48. To quantitatively determine the magnetic interactions in LSMO327, we have calculated the spin-wave dispersion and the differential scattering cross section numerically by applying the Holstein–Primakoff transformation[42] and the Bogoliubov transformation to a Heisenberg model with the in-plane $J_{\parallel}$, *intra*-bilayer $J_{\perp}$, and *inter*-bilayer J' interactions. We found that the exchange interactions systematically change with changing x. Such an x dependence of the exchange interactions is well explained by an orbital liquid picture.

II. EXPERIMENTAL PROCEDURES

LSMO327 powder was prepared by solid-state reaction using prescribed amount of pre-dried La_2O_3 (99.9%), Mn_3O_4 (99.9%), and $SrCO_3$ (99.99%). The powder mixture was calcined in the air. The first firing was carried out at 1250 °C for 24 h. Each additional firing was done for 12–24 h at 25–50 °C higher than the previous firing temperature, then the calcined powder was finely ground and checked with x-ray diffraction. This process was repeated until no trace of foreign phases was observed. The final firing temperatures were 1425 °C for $x=0.3$ and 1375 °C for $x=0.35$–0.48. Note that these sufficiently high firing temperatures are essential to facilitate adequate solid-state reactions for LSMO327.[26] The calcined powder was then pressed into a rod (8 $\phi\times$100 mm) and heated at 1450 °C for 24 h. Single crystals were melt-grown in flowing 100% O_2 in a floating zone optical image furnace with a traveling speed of 15 mm/h. To grow a single-domain crystal, we paid special attention to the stabilization of the floating zone, and employed the necking and seeding techniques repeatedly, both of which are effective in excluding undesired domains.[26] We pulverized several parts of single crystals and checked with x-ray diffraction. All the samples used in the present study show no indication of impurity phases. To check the inhomogeneity along the radial direction, we checked the cross sections (7 cm from the seed) of the $x=0.40$, 0.45, and 0.48 samples with electron probe microanalysis (EPMA). Map scans exhibit no particular spatial inhomogeneity within the instrumental error. The $x=0.30$ sample was examined by inductively coupled plasma (ICP) analysis, which revealed that the ratio of La, Sr, and Mn is 28.6: 32.2: 39.2, which is in good agreement with the ideal ratio, 28.0: 32.0: 40.0. Although stacking faults in the double layered structure may result in the $La_{1-x}Sr_xMnO_3$ and $La_{1-x}Sr_{1+x}MnO_4$ phases, such foreign phases should be no more than 1% of the total volume according to the analyses mentioned above. We thus believe that our samples are sufficiently stoichiometric and homogeneous for measurements of the spin dynamics, which is not very sensitive to a tiny amount of impurities, if any. Similarly grown samples in the range $0.3\leqslant x\leqslant 0.5$ were pulverized and studied in detail by powder neutron diffraction techniques using the Rietveld analysis method. The results were already published in Refs. 27,28. The transport and magnetic properties of the samples were also measured, part of which were published in Refs. 43,44. The results are consistent with previously reported data,[24] which also proves sufficient quality of our samples. The samples cut from the end part of melt-grown rods have a cylindrical shape, which size is typically $5\phi\times 20$–30 mm. We have checked by neutron diffraction that all samples are single domain with a mosaic spread of 0.3°–0.8° full-width-at-half-maximum (FWHM).

Neutron-scattering measurements were carried out using the Tohoku University triple-axis spectrometer TOPAN located in the JRR-3M reactor of the Japan Atomic Energy Research Institute (JAERI). The spectrometer was set up in the standard triple-axis mode with the fixed final energy E_f at 13.5 meV or 14.7 meV and the horizontal collimation of Blank-60′-S-60′-Blank or Blank-100′-S-100′-Blank. The (0 0 2) reflection of pyrolytic graphite (PG) was used to monochromate and analyze the neutron beam, together with a PG filter to eliminate higher order contamination. The sample was mounted in an Al can so as to give the (h 0 l) zone in the tetragonal $I4/mmm$ notation. The Al can was then attached to the cold finger of a closed-cycle He gas refrigerator. All the data were taken at 10 K.

III. RESULTS

As shown by Fujioka *et al.*[38] and Chatterji *et al.*,[39,40] the spin-wave dispersion of LSMO327 with $x=0.4$ should have two modes, i.e., acoustic (A) and optical (O) branches, due to a coupling between layers within a double-layer. It was theoretically shown that the A-branch has maximum intensity at $l=5n$ (n: integer), while the phase of the O-branch is shifted by π in the double-layered system.[38] We thus measured the spin-wave dispersions along [h 0 0] around (1 0 0) and (1 0 5) for the A-branch and around (1 0 2.5) and (1 0 7.5) for the O-branch. To study the differential cross sections of spin waves, we have also measured the l-dependence of the spin-wave intensities of A- and O-branches at a fixed transfer energy $\Delta E=E_i-E_f$.

Figure 2(a) shows the dispersion relations of spin waves at 10 K for $x=0.30$. Error bars correspond to the full-width at half-maximum (FWHM) of peak profiles including the instrumental resolution. The spin waves of the A-branch are well defined in the low momentum (q) and low energy transfer region. However, the O-branch exhibits a large broadening even at the magnetic zone center. The l-dependence of the constant energy scan at $\Delta E=20$ meV is shown in Fig. 3(a). As expected, the A- and O-branches exhibit intensity maxima at $l=5n$ and $l=\frac{5}{2}(2n+1)$. Solid and dotted curves are fitting to theoretical calculations, which are described in the next section.

Figure 2(b) shows the dispersion relations for $x=0.35$. The dispersion curves of both the A- and O-branches become slightly steeper than those of $x=0.30$, indicating that the in-plane magnetic interaction $J_{\parallel}$ increases only gradually. However, the gap between the A- and O-branches becomes almost half of that at $x=0.30$. Since the gap corresponds to the out-of-plane magnetic interaction $J_{\perp}$, this result indicates that $J_{\perp}$ decreases considerably. More quantitative analyses will be made in the following sections. We have

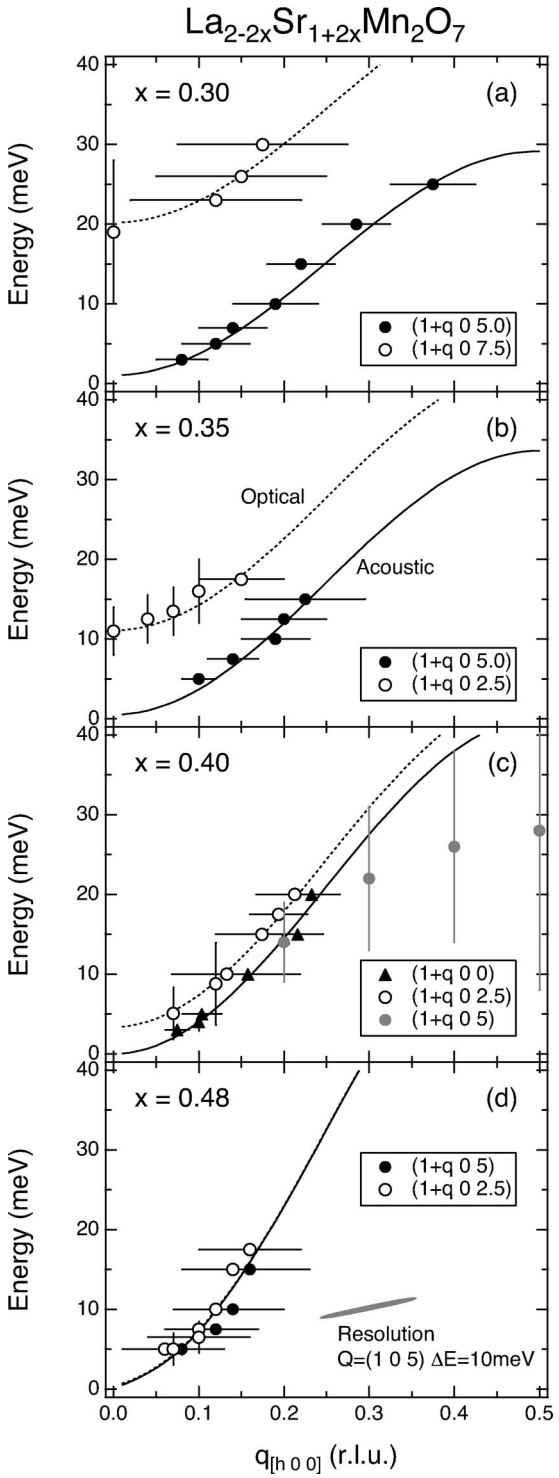

FIG. 2. Dispersion relations of spin waves at 10 K for (a) $x=0.30$, (b) $x=0.35$, (c) $x=0.40$, and (d) $x=0.48$. Error bars correspond to the FWHM of observed peak profiles. A typical resolution function projected onto the $q_{[h00]}$-E plane is drawn in (d) as a gray ellipsoid. Solid circles and open circles indicate the acoustic branch and the optical branch, respectively. Solid and dotted curves are obtained by fitting to theoretical models described in Sec. IV. Note that the $(1+q\ \ 0\ \ 5)$ data for $x=0.40$ are not used for the fitting.

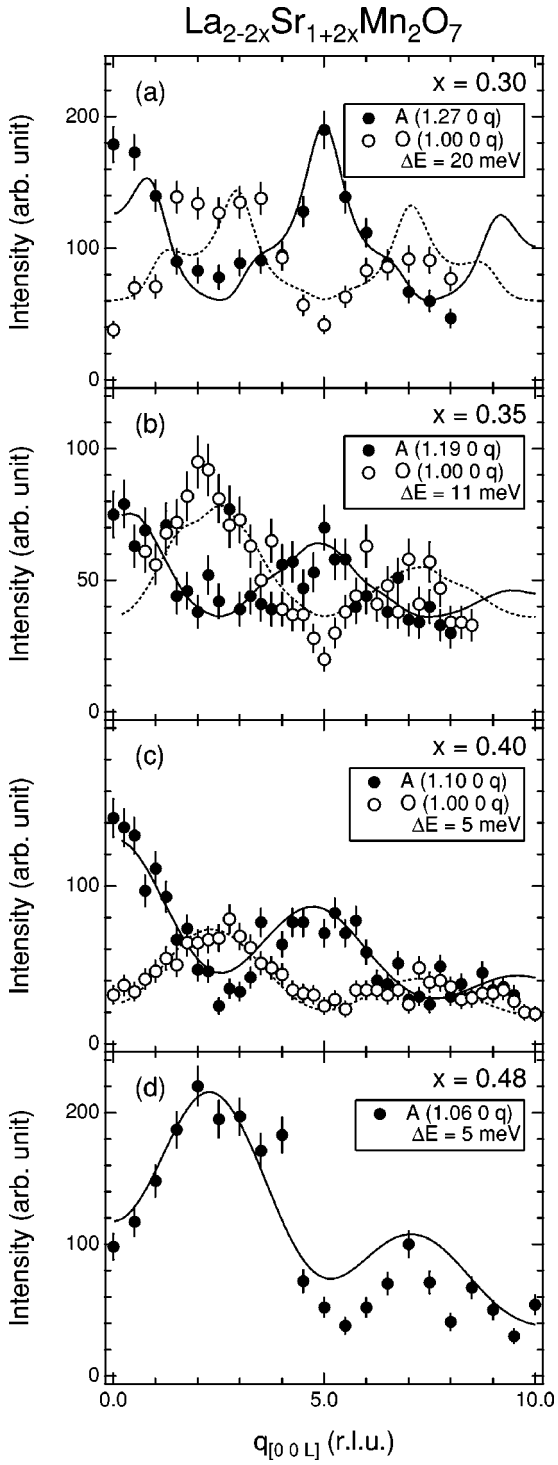

FIG. 3. Differential cross sections along the out-of-plane direction, which were obtained from the l-dependence of the constant E scans. The solid and open circles indicate intensities of the acoustic and optical branches, respectively. Solid and dotted curves are obtained by fitting to theoretical models described in Sec. IV. The acoustic branch is dominant at (1 0 0) and (1 0 5), and the optical branch is dominant at (1 0 2.5) and (1 0 7.5).

also noticed that the spin waves are fairly well defined below 20 meV, and that they becomes significantly broad above 20 meV, even in the constant energy scans. The *l*-dependence at $\Delta E = 11$ meV are shown in Fig. 3(b).

Figure 2(c) shows the dispersion relations for $x = 0.40$. Part of the data has been already reported.[38] The *l*-dependence at $\Delta E = 5$ meV are shown in Fig. 3(c). Following the tendency between $x = 0.30$ and 0.35, the dispersion curves become steeper and the gap becomes smaller. Typical peak profiles of the spin wave of the $x = 0.40$ sample are shown in Fig. 4. Measurement configurations are given in the figures. Figure 4(a) shows constant *E* scans taken at $\Delta E = 5$, 10, and 15 meV along the [100] direction around (1 0 0). Peaks are nearly symmetrical around the (1 0 0) zone center as expected for longitudinal constant *E* scans. Thick gray lines indicate calculated *Q* widths at $\Delta E = 5$ and 10 meV. Energy spectra taken by the constant *Q* method are shown in Figs. 4(b) and 4(c). Thick gray lines indicate calculated *E* widths for $\Delta E = 5$ meV at (1.10 0 0) and 10 meV at (1.12 0 0). As shown in Figs. 4(a) and 4(b), comparison of the peak profiles and the resolution shows that the spin wave is well defined in a low *q* range. However, Fig. 2(c) shows the energy width exhibits anomalous broadening near the zone boundary, which was reported by Fujioka *et al.*[38] The constant *Q* scan at (1.50 0 0) shows a peak around 22 meV on a much broader peak. As is clear from the scans at the zone center, the 22 meV peak is assigned to an optical phonon branch. Furukawa and Hirota[45] investigated this broadening from both theoretical and experimental point of view, and ascribed it to a strong magnon-phonon coupling. Let us consider a dispersionless optical phonon branch at $\hbar\Omega_0$, and a spin-wave dispersion $\hbar\omega(q)$. When a magnon with momentum *q* has energy $\omega(q) > \Omega_0$, it is possible to find an inelastic channel to decay into a magnon-phonon pair with momentum q' and $q - q'$, respectively, which satisfies the energy conservation law, $\omega(q) = \omega(q') + \Omega_0$. This decay channel gives rise to an abrupt broadening of the linewidth of the spin-wave branch which crosses the optical phonon.

Figure 2(d) shows the dispersion relations for $x = 0.48$. The *l*-dependence of the constant energy scan at $\Delta E = 5$ meV are shown in Fig. 3(d). The two branches measured at $(1+q\ \ 0\ \ 5)$ and $(1+q\ \ 0\ \ 2.5)$ nearly degenerate. Unlike $x = 0.30$, 0.35, and 0.40, $x = 0.48$ has the A-type AFM (AFM-I) structure, resulting in a fundamental difference in the spin-wave dispersion. We will discuss this difference in detail in the next section.

As pointed out by Furukawa and Hirota, there exists an optical phonon branch around $\Delta E = 20$ meV for $x = 0.40$ as shown in Fig. 4(c), which we have also confirmed for the other compositions we studied in the present work. We have noticed that the linewidths of spin waves above this characteristic energy of 20 meV become significantly broad, which is consistent with the strong magnon-phonon coupling model mentioned above. Khaliullin and Kilian[46] considered an orbitally degenerate double-exchange system coupled to Jahn–Teller active phonons, which explains the softening of spin waves at the zone boundary found in various ferromagnetic manganese oxides. Their model could be applicable to the anomalous broadening of the spin waves of LSMO327, particularly near the zone boundary. Very recently, Chaboussant *et al.*[47] measured the spin-wave dispersion throughout the Brillouin zone for their $x = 0.40$ sample using time-of-flight (TOF) spectrometers at the ISIS pulsed spallation neutron

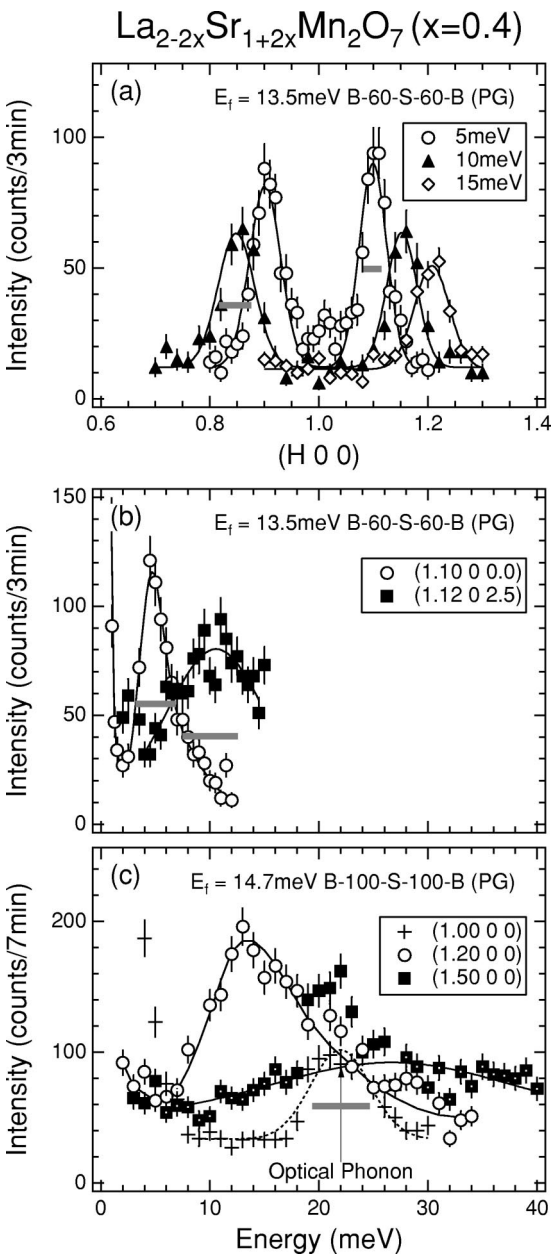

FIG. 4. Typical profiles of the spin wave at 10 K for the $x = 0.40$ sample. (a) Constant *E* scans of the acoustic branch at the energy transfers of $\Delta E = 5$, 10, and 15 meV along the [100] direction at (1 0 0). Solid curves are fit to a double Gaussian. Thick gray lines indicate calculated *Q* widths at $\Delta E = 5$ and 10 meV. (b) Constant *Q* scans at (1.10 0 0) (acoustic) and (1.12 0 2.5), (optical). Lines are guides to the eye. (c) Constant *Q* scans of the acoustic branch at (1.20 0 0) and (1.50 0 0) (zone boundary). An optical phonon branch is shown in the energy spectrum at (1.00 0 0) (zone center). Thick gray lines in (b) and (c) indicate calculated *E* widths for $\Delta E = 5$ meV at (1.10 0 0), 10 meV at (1.12 0 0), and 22 meV at (1 0 0). Overall energy spectra through out the zone are published as an $E - q$ contour map in Ref. 45

source. The effective magnetic exchange interactions they obtained are consistent with previous measurements done by triple-axis spectrometers at research reactors in relatively small transfer energies.[38,39] Although they did not seem to notice broadening around $\Delta E \approx 20$ meV, this may be due to difference between the triple-axis and TOF methods, latter of which measures a scattering function along certain trajectories in the $Q-E$ space and does not give exact constant Q scans. It is, however, clear from their results that the spin wave is observable near the zone boundary along $[\xi\xi 0]$ where the dispersion reaches 80 meV. We thus believe that it is a strong magnon-phonon coupling which principally broadens the spin wave around $\Delta E \approx 20$ meV. In the present paper, we have combined constant Q and E scans to efficiently measure the dispersion relations, which is our principle target of the present work. Constant E scans are particularly useful to avoid contamination from dispersionless optical phonon branches. To further investigate this issue, however, it is necessary to measure the energy widths at various q utilizing constant Q scans, which we plan to carry out in the next step.

IV. THEORETICAL ANALYSIS

In order to analyze the experimental results of the spin-wave dispersion relation and the scattering cross section in LSMO327, we start with the Heisenberg model where $3d$ electrons in a Mn ion are treated as a localized spin. In the FM (A-type AFM) structure for LSMO327 with $x=0.3$, 0.35, and 0.4 ($x=0.48$), a magnetic unit cell includes two (four) Mn ions termed A and B (A, B, C, and D). Between Mn ions, three kinds of exchange interactions, i.e., in-plane $J_\parallel$, intra-bilayer $J_\perp$, and inter-bilayer J' exchange interactions are introduced. A schematic picture is shown in Fig. 1. The Hamiltonian is given by

$$\mathcal{H}=\frac{1}{2}\sum_{il}\mathbf{S}^l(\mathbf{r}_{il})\left\{J_\parallel\sum_{\delta_\parallel}\mathbf{S}^l(\mathbf{r}_{il}+\boldsymbol{\delta}_\parallel)+J_\perp\sum_{\delta_\perp}\mathbf{S}^{l_\perp}(\mathbf{r}_{il}+\boldsymbol{\delta}_\perp)+J'\sum_{\delta'}\mathbf{S}^{l'}(\mathbf{r}_{il}+\boldsymbol{\delta}')\right\}, \tag{1}$$

where $\mathbf{S}^l(\mathbf{r}_{il})$ is the spin operator at the lth Mn ion in the ith unit cell and $\mathbf{r}_{il}$ is the position of the ion. Spin quantum number is assumed to be $S=2(1-x)+\frac{3}{2}x$ with the hole concentration x. $l_\perp=l'=(B,A)$ for $l=(A,B)$ in the FM structure and $l_\perp=(B,D,A,C)$ and $l'=(D,C,B,A)$ for $l=(A,B,C,D)$ in the A-type AFM structure. $\boldsymbol{\delta}_\parallel$, $\boldsymbol{\delta}_\perp$ and $\boldsymbol{\delta}'$ indicate the vectors connecting the NN Mn ions; $\boldsymbol{\delta}_\parallel=(\pm a,0,0)$ and $(0,\pm a,0)$ where a is the distance between NN Mn ions in the ab plane. $\boldsymbol{\delta}_\perp=(0,0,c_\perp)$ and $\boldsymbol{\delta}'=(\pm a/2, \pm a/2,-c')$ for $l=B$ and D, and $\boldsymbol{\delta}_\perp=(0,0,-c_\perp)$ and $\boldsymbol{\delta}'=(\pm a/2,\pm a/2,c')$ for $l=A$ and C, where $c_\perp$ and c' are distances between NN MnO_2 layers and NN bilayers, respectively. By applying the Holstein–Primakoff transformation to Eq. (1), the Hamiltonian is rewritten as follows:

$$\mathcal{H}=\sum_k \psi^\dagger(\mathbf{k})\varepsilon(\mathbf{k})\psi(\mathbf{k}). \tag{2}$$

$\psi(\mathbf{k})=(a_k,b_k)$ for the FM structure and $\psi(\mathbf{k})=(a_k,b_k^\dagger,c_k,d_k^\dagger)$ for the A-type AFM structure, where a_k, b_k, c_k and d_k are the boson operators for the spin operators $\mathbf{S}^A$, $\mathbf{S}^B$, $\mathbf{S}^C$ and $\mathbf{S}^D$, respectively. $\varepsilon(\mathbf{k})$ is given by

$$\varepsilon(\mathbf{k})=\begin{pmatrix} \mathrm{x} & \mathrm{y} \\ \mathrm{y}^* & \mathrm{x}\end{pmatrix}, \tag{3}$$

with

$$\mathrm{x}=-4J_\parallel S\{1-\tfrac{1}{2}(\cos ak_\mathrm{x}+\cos ak_\mathrm{y})\}-J_\perp S-4J'S, \tag{4}$$

and

$$\mathrm{y}=J_\perp S e^{ik_z c_\perp}+4J'S\cos\left(\frac{ak_\mathrm{x}}{2}\right)\cos\left(\frac{ak_\mathrm{y}}{2}\right)e^{ik_z c'}, \tag{5}$$

for the FM structure, and

$$\varepsilon(\mathbf{k})=\begin{pmatrix} X & Y^* & Z & \\ Y & X & & Z^* \\ Z^* & & X & Y \\ & Z & Y^* & X\end{pmatrix}, \tag{6}$$

with

$$X=-4J_\parallel S\{1-\tfrac{1}{2}(\cos ak_\mathrm{x}+\cos ak_\mathrm{y})\}+J_\perp S-4J'S, \tag{7}$$

$$Y=J_\perp S e^{ik_z c_\perp}, \tag{8}$$

and

$$Z=4J'S\cos\left(\frac{ak_\mathrm{x}}{2}\right)\cos\left(\frac{ak_\mathrm{y}}{2}\right)e^{ik_z c'}, \tag{9}$$

for the A-type AFM structure. By utilizing the canonical transformation of the Hamiltonian Eq. (2), the dispersion relations of the spin waves are obtained. On an equal footing, the differential scattering cross section for the inelastic-neutron scattering from spin wave is given by

$$\frac{d^2\sigma}{d\Omega\, d\omega'}=\frac{\gamma e^2}{mc^2}\left(\frac{1}{2}gF(\mathbf{Q})\right)^2\frac{k'}{k}e^{-2W(\mathbf{Q})}N\frac{S}{8}\sum_{ll'm}\sum_{qG}\{\delta(\omega-\omega_q^m)\delta(\mathbf{Q}-\mathbf{G}-\mathbf{q})(1+n_q^m)U_{lm}^\dagger(\mathbf{q})U_{ml'}(\mathbf{q}) + \delta(\omega+\omega_q^m)\delta(\mathbf{Q}-\mathbf{G}+\mathbf{q})n_q^m U_{lm}(\mathbf{q})U_{ml'}^\dagger(\mathbf{q})\}, \tag{10}$$

where $\mathbf{q}$ and ω_q^m are the momentum and energy of spin wave of the mode m, respectively, and $n_q^m=1/(e^{\beta\omega_q^m}-1)$ is a Bose factor with temperature $T=1/\beta$. $U(\mathbf{q})$ is a matrix introduced in the canonical transformation. $\mathbf{Q}=\mathbf{k}_i-\mathbf{k}_f$ is the momentum transfer, where $\mathbf{k}_i$ and $\mathbf{k}_f$ are the momenta of the incident and scattered neutrons. $\mathbf{G}$ is a reciprocal lattice vector. $F(Q)$ and $W(Q)$ are the magnetic structure factor and the Debye–Waller factor, respectively.

The experimental results of the dispersion relation and the differential scattering cross section in LSMO327 are fitted by

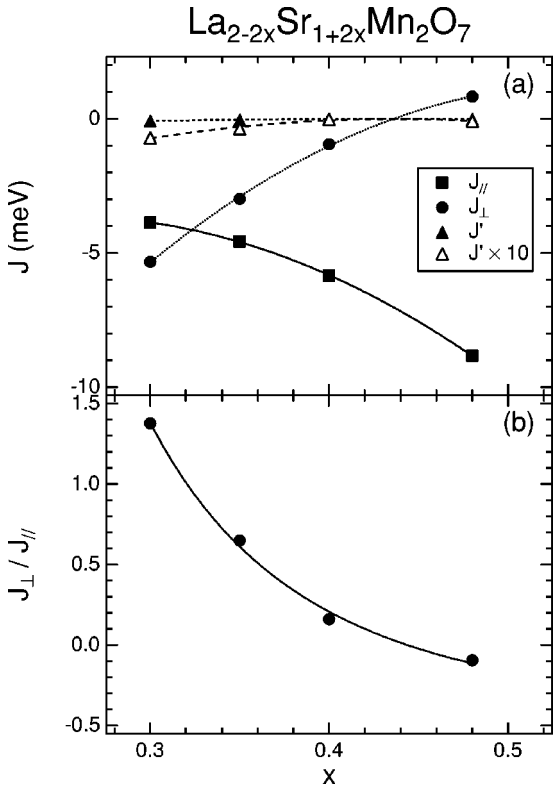

FIG. 5. (a) x dependence of the exchange interactions obtained by analyses of the dispersion relations and the scattering cross sections in the inelastic neutron scattering experiments. (b) x dependence of the ratio of the exchange interactions $J_\perp$ and $J_\parallel$.

utilizing the least-squares method. The calculated results are shown in Figs. 2 and 3 together with the experimental data. Note that the dispersion relation along $[h\ 0\ 0]$ and the cross section along $[0\ 0\ l]$ are sensitive to $J_\parallel$, $J_\perp$, and J'. In the case of $x=0.3$, 0.35, and 0.4, the A- and O-branches are well separated. These two correspond to the in-phase and out-of phase motions of spins in NN MnO_2 layers. The energy separation between the two branches at the point Γ and the stiffness constant of the A-branch in the ab plane are given by $-2S(J_\perp+4J')$ and $D=-SJ_\parallel$, respectively. The intensity oscillations along $[0\ 0\ l]$ are factorized by the functions $1+\cos(c_\perp q_z)$ and $1-\cos(c_\perp q_z)$ for the A- and O-branches, respectively, where $c_\perp$ is approximately 1/5 of c, the lattice constant along the c axis. This is attributed to the spin correlation between NN MnO_2 layers controlled by $J_\perp$. Additional fine structures in the intensity are caused by J'. In the A-type AFM structure, on the contrary, four modes of the spin wave exist and separate into the A- and O-branches corresponding to the in-phase and out-of phase motions of spins between NN bilayers. Here, each branch is doubly degenerate and the energy separation between the two is of the order of J'. Since $J'\sim J_\parallel/1000$ at $x=0.48$, as mentioned later, they cannot be observed separately in experiments. An intensity oscillation along [0 0 l] is factorized by a function $1-\cos(c_\perp q_z)$ originating from the antiferromagnetic spin alignment between the NN MnO_2 layers.

The x dependence of the exchange interactions is shown in Fig. 5. All interactions systematically change with x; with increasing x from 0.3, $|J_\parallel|$ increases and $J_\perp$ rapidly approaches zero then changes its sign from negative to positive. $|J'|$ decreases with increasing x, and its value is 100–1000 times smaller than $|J_\parallel|$ and $|J_\perp|$. The systematic change of the interactions correlates with that of the distortion of MnO_6 octahedra represented by Δ_{JT}, which continuously decreases from 1.035 at $x=0.30$ to 1.005 at $x=0.50$.[28] This is, however, contrary to what expected from the conventional double-exchange scenario: $|J_\parallel|$ is reduced with increasing x because, in the strong Hund-coupling limit, the magnitude of the double-exchange interaction is proportional to the hopping integral between Mn ions, thus to the Mn–O bond length. Therefore, a structural change itself cannot account for that of the exchange interactions. Let us taking into account the orbital degree of freedom in a Mn ion. In LSMO327 with the hole concentration x, $1-x$ electrons occupy the two e_g orbitals. The character of the occupied orbital controls the anisotropy of the hopping integral of electrons, i.e., that of the ferromagnetic double exchange interaction. The systematic change of the exchange interactions can be explained by assuming that the $3d_{x^2-y^2}$ orbital is relatively stabilized with increasing x. The exchange interaction between Mn ions is a sum of the ferromagnetic double-exchange interaction and the antiferromagnetic superexchange interaction (J_{AFM}) acting between t_{2g} spins. The more the $d_{x^2-y^2}$ orbital is stabilized, the more the ferromagnetic interaction becomes strong in the ab plane and weak along the c axis. Then J_{AFM} overcomes the ferromagnetic interaction along the c axis as shown in the region of $x=0.4$–0.48. This assumption for the orbital stability is consistent with the x dependent Δ_{JT},[28,34,35] and is supported by the previous theoretical work where the stability of the orbitals is examined by the Madelung potential calculation.[48,49]

V. DISCUSSION AND SUMMARY

Let us discuss possible orbital states in LSMO327 with $0.3\leqslant x<0.5$ and its relation to the anisotropy of the ferromagnetic interaction in more detail. The orbital state at each Mn ion is represented by the pseudo-spin operator defined by

$$T_{i\mu}=\frac{1}{2}\sum_{s\gamma\gamma'} d^\dagger_{i\gamma s}\sigma_\mu d_{i\gamma' s}, \tag{11}$$

for $\mu=(x,z)$. $d_{i\gamma s}$ is the annihilation operator for the e_g electron at site i with spin s and orbital γ, and σ_μ are the Pauli matrices. In the eigen state of $T_{iz}=+(-)1/2$, an electron occupies the $d_{3z^2-r^2}$ ($d_{x^2-y^2}$) orbital at site i. T_{iz} (T_{ix}) describes the charge quadrupole moment with tetragonal (orthorhombic) symmetries and couples with the lattice distortion with the same symmetry;

$$\mathcal{H}_{JT}=-g\sum_{i\mu=x,z} T_{i\mu}Q_{i\mu}, \tag{12}$$

where Q_{iz} and Q_{ix} describe displacements of the O ions in a MnO_6 octahedron. The orbital ordered state is characterized by a magnitude and an angle of this operator, i.e., $|\langle\mathbf{T}\rangle|=\sqrt{\langle T_x\rangle^2+\langle T_z\rangle^2}$ and $\Theta=\tan^{-1}(\langle T_x\rangle/\langle T_z\rangle)$ where $\langle\cdots\rangle$ is a

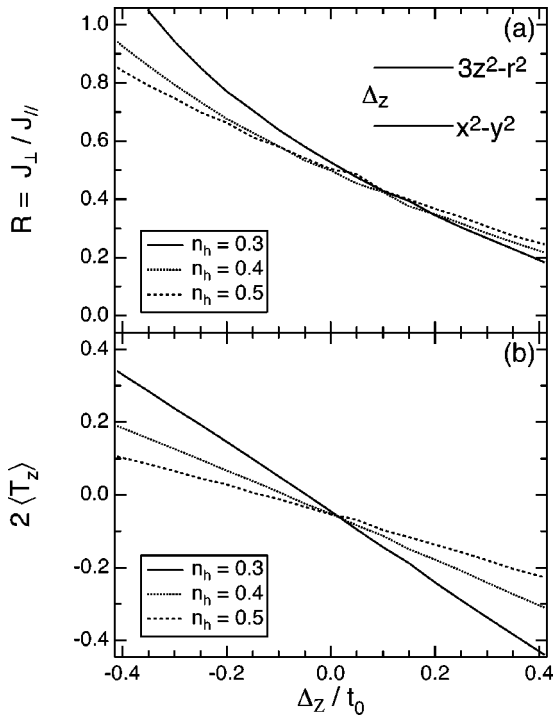

FIG. 6. (a) Theoretical results of the exchange interactions ratio $R=J_\perp/J_\parallel$. $J_\parallel$ and $J_\perp$ are the exchange interactions between NN Mn sites in the ab plane and along the c direction, respectively. (inset) Δ_z is the splitting of the energy levels of the $d_{3z^2-r^2}$ and $d_{x^2-y^2}$ states. (b) Relative number of occupied electrons in two e_g orbitals $2\langle T_z\rangle$.

thermal average. For example, in the $(d_{3x^2-r^2}, d_{3y^2-r^2})$-type orbital ordered state in $LaMnO_3$, we obtain $\Theta=2\pi/3$ and $-2\pi/3$ for the Mn sites where the $d_{3x^2-r^2}$ and $d_{3y^2-r^2}$ orbitals are occupied, respectively.

As mentioned in the previous section, a relative weight of the occupied $d_{x^2-y^2}$ orbital increases continuously with increasing x from 0.3 to 0.48 in LSMO327 where the crystal structure remains tetragonal ($I4/mmm$). That is, $\langle T_z(\mathbf{k}=0)\rangle$ is gradually reduced while keeping the condition $\langle T_x(\mathbf{k}=0)\rangle=0$ where $\mathbf{T}(\mathbf{k})=1/N\Sigma_i e^{i\mathbf{k}\cdot\mathbf{r}_i}\mathbf{T}_i$ with the number of Mn ions N and the position of the ith ion $\mathbf{r}_i$. This cannot be satisfied by a uniform orbital ordered state, where a particular orbital state characterized by Θ occupies all Mn sites. This is because the change of the orbital state is represented by the rotation of $\langle\mathbf{T}\rangle$ in the $\langle T_z\rangle$-$\langle T_x\rangle$ plane. One might think that the experimental results are explained with an antiferro-type orbital ordered state, in which the condition $\Theta_A=-\Theta_B$ is satisfied in the orbital space for the A and B sublattices. However, this is ruled out by the experimental fact that the expected superlattice reflection was not reported in $0.3\leqslant x<0.5$ by the x-ray and electron diffractions.[50,51]

One of the possible orbital states realized in LSMO327 is an *orbital liquid* state. This state was originally proposed in the ferromagnetic metallic state of LSMO113 in Ref. 52, where the ordered states of both T_z and T_x are suppressed by the low-dimensional character of orbital fluctuations. In the case of LSMO327, $\langle T_z\rangle$ is finite due to the layered crystal

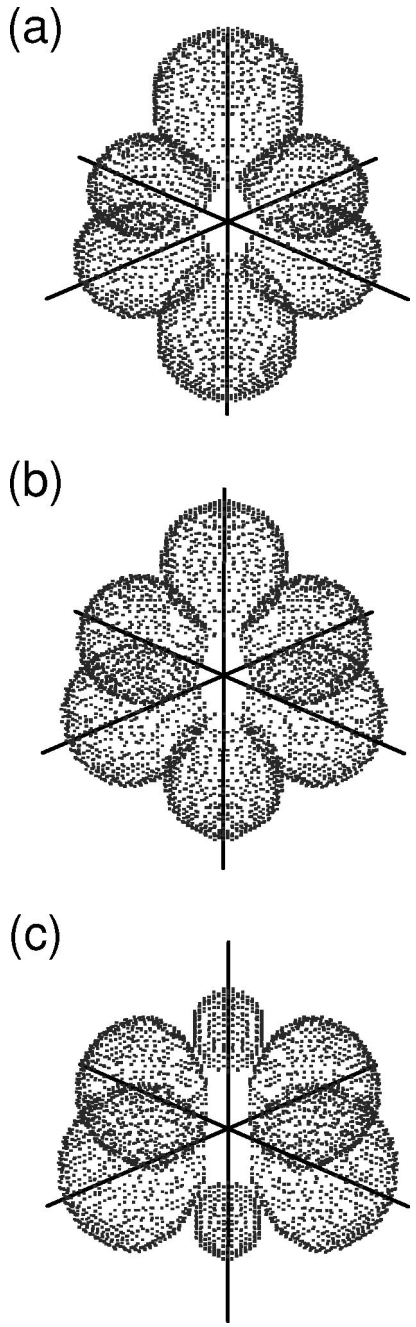

FIG. 7. Schematic pictures of the charge distribution for e_g electrons in the case of (a) $\Delta_z=-0.4$, (b) 0, and (c) 0.4.

structure. On the other hand, T_{ix} does not show ordering and symmetry for the charge distribution remains tetragonal at each Mn site. In order to formulate this orbital state, let us start with the Hamiltonian where the intra-site Coulomb interactions in Mn ions are taken into account;

$$\mathcal{H}=\sum_{\langle ij\rangle\sigma}(t_{ij}^{\gamma\gamma'}\tilde{d}_{i\gamma\sigma}^{\dagger}\tilde{d}_{j\gamma'\sigma}+H.c.)-J_H\sum_i \mathbf{S}_i\cdot\mathbf{S}_{ti}+\Delta_z\sum_i T_{iz}, \tag{13}$$

where $\tilde{d}_{i\gamma\sigma}=d_{i\gamma\sigma}(1-n_{i\gamma\bar{\sigma}})(1-n_{i\bar{\gamma}\sigma})(1-n_{i\bar{\gamma}\bar{\sigma}})$ is the annihilation operator of an e_g electron excluding the doubly oc-

cupied states of electrons due to the strong Coulomb interaction. $\mathbf{S}_i$ is the spin operator for an e_g electron defined by $\mathbf{S}_i=\frac{1}{2}\Sigma_{ss',\gamma}d^{\dagger}_{i\gamma s}\boldsymbol{\sigma}_{ss'}d_{i\gamma s'}$ and $\mathbf{S}_{ti}$ is the spin operator for t_{2g} electrons with $S=3/2$. The first and second terms in Eq. (13) represent the hopping of e_g electrons between NN Mn sites and the Hund-coupling between e_g and t_{2g} spins, respectively. The splitting between the energy levels of the $d_{3z^2-r^2}$ and $d_{x^2-y^2}$ orbitals due to a tetragonal distortion of a MnO_6 octahedron is represented by Δ_z in the third term as $\Delta_z=\varepsilon_{3z^2-r^2}-\varepsilon_{x^2-y^2}$. It is shown from the theoretical calculation in Ref. 49 that Δ_z monotonically increases with increasing x for LSMO327 and its maximum value is of the order of 0.5 eV. Instead of considering the actual crystal structure of LSMO327, a pair of the 2D sheets, where a squared lattice consists of Mn ions is employed because of the weak interbilayer exchange interaction. We adopt the slave-boson scheme where $\tilde{d}_{i\gamma\sigma}$ is decomposed into a product of operators: $\tilde{d}_{i\gamma\sigma}=f^{\dagger}_i\tau_{i\gamma}s_{i\sigma}$ where f_i and $s_{i\sigma}$ are bosonic operators for charge and spin degrees of freedom, respectively, and $\tau_{i\gamma}$ is a fermionic one for orbital associated with the constraint of $\Sigma_\sigma s^{\dagger}_{i\sigma}s_{i\sigma}=\Sigma_\gamma\tau^{\dagger}_{i\gamma}\tau_{i\gamma}$ and $f^{\dagger}_i f_i+\Sigma_\sigma s^{\dagger}_{i\sigma}s_{i\sigma}=1$ at each site.[53] The mean field approximation is introduced; $\langle f^{\dagger}_i f_j\rangle=x$ and $\Sigma_\sigma\langle s^{\dagger}_{i\sigma}s_{j\sigma}\rangle=(1-x)\varepsilon_{ij}$ with $\varepsilon_{ij}=+(-)1$ for a ferromagnetic (antiferromagnetic) bond in the orbital part of the mean-field Hamiltonian. It is well known that the slave-boson mean-field approximation is suitable for describing the spin liquid state.[54] The ratio of the ferromagnetic exchange interaction along the c-axis to that in the ab plane is given by $R=J_\perp/J_\parallel=\chi_c/\chi_{ab}$ with $\chi_l=\Sigma_{\gamma\gamma'}\langle\tau^{\dagger}_{i\gamma}\tau_{i+l\gamma'}\rangle$ for $l=ab$ and c. The results are shown in Fig. 6(a) where J_H is assumed to be infinite and t_0 is the hopping integral between the $d_{3z^2-r^2}$ orbitals in the c axis. R continuously decreases with increasing Δ_z implying that $d_{x^2-y^2}$ orbital becomes stable relatively. This feature does not depend on the hole concentration n_h in the calculation. Since Δ_z is expected to continuously increase with increasing x in LSMO327, the results in Fig. 6(a) explain the experimental results presented in Fig. 5(b). The Δ_z dependence of $\langle T_z\rangle$ are shown in Fig. 6(b). We note that $\langle T_x\rangle$ is zero. It is clearly shown that the continuous change of R is controlled by the character of the occupied orbital. We also present the schematic pictures of the spatial distribution of the electronic charge at a Mn site in Fig. 7 for the proposed orbital liquid state. The charge distributions have tetragonal symmetry and are not represented by any linear combination of the atomic wave functions of the $d_{3z^2-r^2}$ and $d_{x^2-y^2}$ orbitals.

To summarize, we have systematically studied low-temperature spin dynamics of the double-layered perovskite $La_{2-2x}Sr_{1+2x}Mn_2O_7$ $(0.3\leqslant x<0.5)$. The acoustic and optical branches of the 2D spin-wave dispersion relations as well as characteristic intensity oscillations along the out-of-plane direction are successfully explained theoretically assuming the Heisenberg models with the in-plane ($J_\parallel$), *intra*-bilayer ($J_\perp$), and *inter*-bilayer (J') exchange interactions. We have found that the ratio $R=J_\perp/J_\parallel$ drastically decreases upon doping holes, which indicates that the $d_{x^2-y^2}$ orbital becomes more stable than the $d_{3z^2-r^2}$ orbital. Note that a simple linear combination of the two states results in an orbital state with an orthorhombic symmetry, inconsistent with the $I4/mmm$ tetragonal symmetry of $La_{2-2x}Sr_{1+2x}Mn_2O_7$. Thus we have introduced an ''orbital liquid'' state, in which the symmetry of the charge distribution is kept tetragonal around each Mn site.

ACKNOWLEDGMENTS

The authors would like to thank S. Okamoto, G. Khaliullin, A. Koizumi, Y. Murakami, and K. Takahashi for their valuable discussions. This work was supported by the Grant in Aid from Ministry of Education, Science and Culture of Japan, CREST, NEDO, and Science and Technology Special Coordination Fund for Promoting Science and Technology. Part of the numerical calculation was performed in the HITACS-3800/380 supercomputing facilities in IMR, Tohoku University.

*Corresponding author: email address: hirota@iiyo.phys.tohoku.ac.jp

†Present address: Department of Applied Physics, University of Tokyo. 7-3-1 Hongo, Tokyo 113-8656, Japan.

‡Present address: Elpida Memoty, Inc., 1120 Shimokuzawa, Sagamihara, Kanagawa, 229-1198, Japan.

§Present address: Photon Factory, Institute of Materials Structure Science, KEK, Tsukuba 305-0801, Japan.

[1] R. M. Kusters, D. A. Singleton, R. Mcgreevy, and W. Hayes, Physica B **155**, 362 (1989).

[2] K. Chabara, T. Ohno, M. Kasai, and Y. Kozono, Appl. Phys. Lett. **62**, 780 (1993).

[3] S. Jin, T. H. Tiefel, M. McCormack, R. A. Fatsnacht, R. Ramesh, and L. H. Chen, Science **264**, 413 (1994).

[4] Y. Tokura, A. Urushibara, Y. Moritomo, T. Arima, A. Asamitsu, G. Kido, and N. Furukawa, J. Phys. Soc. Jpn. **63**, 3931 (1994).

[5] A. Urushibara, Y. Moritomo, T. Arima, A. Asamitsu, G. Kido, and Y. Tokura, Phys. Rev. B **51**, 14103 (1995).

[6] H. Y. Hwang, S.-W. Cheong, P. G. Radaelli, M. Marezio, and B. Batlogg, Phys. Rev. Lett. **75**, 914 (1995).

[7] *Colossal Magnetoresistance, Charge Ordering, and Related Properties of Manganese Oxides*, edited by C.N.R. Rao and B. Raveau (World Scientific, Singapore, 1998).

[8] M. Imada, A. Fujimori, and Y. Tokura, Rev. Mod. Phys. **70**, 1039 (1998).

[9] *Physics of manganites*, edited by T. A. Kaplan and S. D. Mahanti (Kluwer Academic/Plenum, New York, 1999).

[10] *Colossal Magnetoresistance Oxides*, edited by Y. Tokura (Gordon and Breach, New York, 2000).

[11] Y. Tokura and N. Nagaosa, Science **288**, 462 (2000).

[12] J. Akimitsu and Y. Ito, J. Phys. Soc. Jpn. **40**, 1621 (1976).

[13] Y. Murakami, H. Kawada, H. Kawata, M. Tanaka, T. Arima, Y. Moritomo, and Y. Tokura, Phys. Rev. Lett. **80**, 1932 (1998).

[14] Y. Murakami, J. P. Hill, D. Gibbs, M. Blume, I. Koyama, M. Tanaka, H. Kawata, T. Arima, Y. Tokura, K. Hirota, and Y. Endoh, Phys. Rev. Lett. **81**, 582 (1998).

[15] K. Hirota, N. Kaneko, A. Nishizawa, and Y. Endoh, J. Phys. Soc. Jpn. **65**, 3736 (1996).

[16] F. Moussa, M. Hennion, J. Rodriguez-Caravajal, H. Moudden, L. Pinsard, and A. Revcolevschi, Phys. Rev. B **54**, 15149 (1996).
[17] I. Solovyev, N. Hamada, and K. Terakura, Phys. Rev. Lett. **76**, 4825 (1996).
[18] S. Ishihara, J. Inoue, and S. Maekawa, Physica C **263**, 130 (1996); Phys. Rev. B **55**, 8280 (1997).
[19] J. B. Goodenough and J. M. Longon, *Landolt-Börnstein Tabelllen Vol. III/4a* (Springer, Berlin, 1970).
[20] H. Kawano, R. Kajimoto, M. Kubota, and H. Yoshizawa, Phys. Rev. B **53**, R14709 (1996).
[21] J. Rodriguez-Caravajal, M. Hennion, F. Moussa, A. H. Moudden, L. Pinsard, and A. Revcolevschi, Phys. Rev. B **57**, R3189 (1998).
[22] A. Asamitsu, Y. Moritomo, Y. Tomioka, T. Arima, and Y. Tokura, Nature (London) **373**, 407 (1995).
[23] D. E. Cox, T. Iglesias, E. Moshopoulou, K. Hirota, K. Takahashi, and Y. Endoh, Phys. Rev. B **64**, 024431 (2001).
[24] Y. Moritomo, A. Asamitsu, H. Kuwahara, and Y. Tokura, Nature (London) **380**, 141 (1996).
[25] For a review, T. Kimura and Y. Tokura, Annu. Rev. Mater. Sci. **30**, 451 (2000).
[26] K. Hirota, Y. Moritomo, H. Fujioka, M. Kubota, H. Yoshizawa, and Y. Endoh, J. Phys. Soc. Jpn. **67**, 3380 (1998); **68**, 1463 (1999).
[27] M. Kubota, H. Fujioka, K. Ohoyama, K. Hirota, Y. Moritomo, H. Yoshizawa, and Y. Endoh, J. Phys. Chem. Solids **60**, 1161 (1999).
[28] M. Kubota, H. Fujioka, K. Hirota, K. Ohoyama, Y. Moritomo, H. Yoshizawa, and Y. Endoh, J. Phys. Soc. Jpn. **69**, 1986 (2000).
[29] M. Kubota, H. Yoshizawa, Y. Moritomo, H. Fujioka, K. Hirota, and Y. Endoh, J. Phys. Soc. Jpn. **68**, 2202 (1999).
[30] D. N. Argyriou, H. N. Bordallo, B. J. Campbell, A. K. Cheetham, D. E. Cox, J. S. Gardner, K. Hanif, A. dos Santos, and G. F. Strouse, Phys. Rev. B **61**, 15269 (2000).
[31] J. F. Mitchell, D. N. Argyriou, J. D. Jorgensen, D. G. Hinks, C. D. Potter, and S. D. Bader, Phys. Rev. B **55**, 63 (1997).
[32] D. N. Argyriou, H. N. Bordallo, J. F. Mitchell, J. D. Jorgensen, and G. F. Strouse, Phys. Rev. B **60**, 6200 (1999).
[33] C. D. Ling, J. E. Millburn, J. F. Mitchell, D. N. Argyriou, J. Linton, and H. N. Bordallo, Phys. Rev. B **62**, 15096 (2000).
[34] T. Kimura, Y. Tomioka, A. Asamitsu, and Y. Tokura, Phys. Rev. Lett. **81**, 5920 (1998).
[35] M. Medarde, J. F. Mitchell, J. E. Millburn, S. Short, and J. D. Jorgensen, Phys. Rev. Lett. **83**, 1223 (1999).
[36] Y. Moritomo, Y. Maruyama, T. Akimoto, and A. Nakamura, J. Phys. Soc. Jpn. **67**, 405 (1998).
[37] T. Okuda, T. Kimura, H. Kuwahara, Y. Tomioka, A. Asamitsu, Y. Okimoto, E. Saitoh, and Y. Tokura, Mater. Sci. Eng., B **63**, 163 (1999).
[38] H. Fujioka, M. Kubota, K. Hirota, H. Yoshizawa, Y. Moritomo, and Y. Endoh, J. Phys. Chem. Solids **60**, 1165 (1999).
[39] T. Chatterji, L. P. Regnault, P. Thalmeier, R. Suryanarayanan, G. Dhalenne, and A. Revcolevschi, Phys. Rev. B **60**, R6965 (1999).
[40] T. Chatterji, P. Thalmeier, G. J. McIntyre, R. van de Kamp, R. Suryanarayanan, G. Dhalenne, and A. Revcolevschi, Europhys. Lett. **46**, 801 (1999).
[41] S. Rosenkranz, R. Osborn, J. F. Mitchell, L. Vasiliu-Doloc, J. W. Lynn, and S. K. Sinha, J. Appl. Phys. **87**, 5816 (2000).
[42] T. Holstein and H. Primakoff, Phys. Rev. **58**, 1094 (1940).
[43] M. Kubota, Y. Oohara, H. Yoshizawa, H. Fujioka, K. Shimizu, K. Hirota, Y. Moritomo, and Y. Endoh, J. Phys. Soc. Jpn. **69**, 1986 (2000).
[44] Y. Moritomo, K. Hirota, H. Nakao, T. Kiyama, Y. Murakami, S. Okamoto, S. Ishihara, S. Maekawa, M. Kubota, and H. Yoshizawa, Phys. Rev. B **62**, 17 (2000).
[45] N. Furukawa and K. Hirota, Physica B **291**, 324 (2000).
[46] G. Khaliullin and R. Kilian, Phys. Rev. B **61**, 3494 (2000).
[47] G. Chaboussant, T. G. Perring, G. Aeppli, and Y. Tokura, Physica B **276-278**, 801 (2000).
[48] T. Akimoto, Y. Moritomo, K. Ohoyama, O. Okamoto, S. Ishihara, S. Maekawa, and A. Nakamura, Phys. Rev. B **59**, R14153 (1999).
[49] S. Okamoto, S. Ishihara, and S. Maekawa, Phys. Rev. B **63**, 104401 (2001).
[50] J. Q. Li, Y. Matsui, T. Kimura, and Y. Tokura, Phys. Rev. B **57**, R3205 (1998).
[51] Y. Wakabayashi, Y. Murakami, I. Koyama, T. Kimura, Y. Tokura, Y. Moritomo, K. Hirota, and Y. Endoh, J. Phys. Soc. Jpn. **69**, 2731 (2000).
[52] S. Ishihara, M. Yamanaka, and N. Nagaosa, Phys. Rev. B **56**, 686 (1997).
[53] R. Kilian and G. Khaliullin, Phys. Rev. B **58**, R11841 (1998).
[54] A. M. Tsvelik, *Quantum Field Theory in Condensed Matter Physics* (Cambridge University Press, Cambridge, 1995).